

# Catalysis Science & Technology

Accepted Manuscript



This is an *Accepted Manuscript*, which has been through the Royal Society of Chemistry peer review process and has been accepted for publication.

*Accepted Manuscripts* are published online shortly after acceptance, before technical editing, formatting and proof reading. Using this free service, authors can make their results available to the community, in citable form, before we publish the edited article. We will replace this *Accepted Manuscript* with the edited and formatted *Advance Article* as soon as it is available.

You can find more information about *Accepted Manuscripts* in the [Information for Authors](#).

Please note that technical editing may introduce minor changes to the text and/or graphics, which may alter content. The journal's standard [Terms & Conditions](#) and the [Ethical guidelines](#) still apply. In no event shall the Royal Society of Chemistry be held responsible for any errors or omissions in this *Accepted Manuscript* or any consequences arising from the use of any information it contains.



Journal Name

ARTICLE

## Nickel sulfides for electrocatalytic hydrogen evolution under alkaline conditions: a case study of crystalline NiS, NiS<sub>2</sub>, and Ni<sub>3</sub>S<sub>2</sub> nanoparticles

Received 00th January 20xx,  
Accepted 00th January 20xx

DOI: 10.1039/x0xx00000x

www.rsc.org/

Nan Jiang,<sup>a</sup> Qing Tang,<sup>b</sup> Meili Sheng,<sup>a</sup> Bo You,<sup>a</sup> De-en Jiang,<sup>b</sup> and Yujie Sun\*<sup>a</sup>

Electrocatalytic water splitting to produce H<sub>2</sub> plays an important role in the capture, conversion, and storage of renewable energy sources, such as solar and wind. As the reductive half reaction of water splitting, the H<sub>2</sub> evolution reaction (HER) suffers from sluggish kinetics and hence competent HER catalysts are needed. Despite being excellent HER catalysts, noble metal-based catalysts (*i.e.* Pt) are too expensive to be economically competitive. Therefore, low-cost catalysts comprised of solely earth-abundant elements have attracted increasing attention these years, among which nickel-based HER catalysts, particularly nickel chalcogenides, are considered as promising candidates. Although many nickel chalcogenides, including NiS, NiS<sub>2</sub>, and Ni<sub>3</sub>S<sub>2</sub>, have been reported for hydrogen evolution, their intrinsic catalytic activities have never been investigated and compared in detail under the same condition. Most previous investigations were limited to only one species of nickel chalcogenides under very unique conditions, rendering a fair comparison of their HER activities impossible. Herein we report the preparation and characterization of three crystalline nickel sulfides, NiS, NiS<sub>2</sub>, and Ni<sub>3</sub>S<sub>2</sub>, with comparable crystal sizes and specific surface areas. Detailed electrochemical studies under strongly alkaline conditions coupled with theoretical computation were performed to probe their intrinsic HER activities, resulting in the order of Ni<sub>3</sub>S<sub>2</sub> > NiS<sub>2</sub> > NiS. The superior HER performance of Ni<sub>3</sub>S<sub>2</sub> mainly stems from the combined effect of large electrochemically active surface area and high conductivity (metallic conductor *vs.* semiconductor).

### Introduction

Water spitting with renewable energy input to produce H<sub>2</sub> and O<sub>2</sub> has been widely considered as a promising approach to alleviate our reliance on fossil fuels, match growing energy demand, and simultaneously satisfy increasingly stringent environmental regulations because of the clean nature of H<sub>2</sub> as a fuel.<sup>1-3</sup> Water splitting consists of two half reactions: H<sub>2</sub> evolution reaction (HER) and O<sub>2</sub> evolution reaction (OER), both of which are multi-electron/multi-proton transfer processes and require catalysts to proceed at appreciable rates.<sup>4</sup> State-of-the-art HER catalysts are usually composed of noble metals, such as Pt, whose limited reserve and thus high cost limit their large-scale applications. Hence, there remains an urgent need to develop competent and earth-abundant HER catalysts prepared by low-cost methods.

Recent years have witnessed the emergence of a wide library of solid-state catalysts comprised of earth-abundant elements, such as metal chalcogenides,<sup>5-7</sup> carbides,<sup>8-13</sup> borides,<sup>8</sup>

and alloys.<sup>14</sup> First-row transition metals are also frequently reported with competent HER activities; noteworthy examples include metal sulfides,<sup>15,16</sup> selenides,<sup>17,18</sup> and phosphides.<sup>19,20</sup> Owing to the thermodynamic convenience and potential application in proton exchange membrane electrolyzers, most reported HER catalysts were developed and investigated under strongly acidic conditions. The preparation of these catalysts typically requires toxic gas treatment at elevated temperature. To eventually realize overall water splitting catalysis, the integration of HER and OER catalysts in the same electrolyte is mandatory. Because the overpotential loss of OER in acidic electrolyte is much larger than that of HER in basic media and most OER catalysts are vulnerable in acidic electrolyte, our group is particularly interested in developing and understanding high-performance HER catalysts under alkaline conditions.<sup>21</sup>

Due to its terrestrial abundance and involvement in [NiFe] hydrogenases,<sup>22</sup> nickel has long been sought as a promising candidate for HER catalysis. Indeed, a variety of nickel-based catalysts have emerged for electrocatalytic H<sub>2</sub> production recently. Typical examples include nickel alloys,<sup>14,23</sup> sulfides,<sup>24-26</sup> selenides,<sup>27</sup> oxides/hydroxides,<sup>28</sup> and phosphides,<sup>29</sup> among which nickel sulfides are one of the most investigated because of its low cost, facile preparation, and high catalytic activity. In fact, many nickel sulfide-based HER catalysts of different crystal structures have been reported for H<sub>2</sub> evolution under either acidic, neutral, or alkaline conditions. For instance, metal organic framework-derived NiS nanoframes

<sup>a</sup> Department of Chemistry and Biochemistry, Utah State University, Logan, Utah 84322, USA. E-mail: yujie.sun@usu.edu; Fax: +1-435-797-3390; Tel: +1-435-797-7608.

<sup>b</sup> Department of Chemistry, University of California, Riverside, California 92521, USA.

† Electronic supplementary information (ESI) available: Additional electrochemistry and characterization data, Figures S1–s4 and Table S1. See DOI: 10.1039/x0xx00000x

have been demonstrated as HER catalysts in 1.0 M KOH.<sup>25</sup> Similarly, NiS<sub>2</sub> of various nanostructures were reported to exhibit remarkable HER catalytic performance in strongly acidic electrolyte.<sup>30,31</sup> Last year, our group reported an electrodeposited Ni-S film with active and robust HER activity not only in neutral buffer but also in natural water.<sup>32</sup> A suite of characterization techniques, including X-ray absorption spectroscopy, were conducted and the main composition of the Ni-S film was revealed to be Ni<sub>3</sub>S<sub>2</sub>.<sup>32</sup> This was the first time that Ni<sub>3</sub>S<sub>2</sub> was found to be a competent HER catalyst. Although the three main crystalline forms of nickel sulfides, NiS, NiS<sub>2</sub>, and Ni<sub>3</sub>S<sub>2</sub>, have all been separately studied as HER catalysts, a fair comparison of their performance on an equal footing has been challenging because of the diverse conditions employed in the aforementioned and other related studies. In order to gain a deeper understanding of their intrinsic HER activities, it is necessary to examine them under the same conditions in order to build a composition-structure-performance relationship of nickel sulfides for the development of improved HER catalysts.

Herein, we report a facile and novel microwave-assisted preparation of three crystalline nickel sulfides, NiS, NiS<sub>2</sub>, and Ni<sub>3</sub>S<sub>2</sub>. Various physical characterization techniques were conducted to confirm that their crystal sizes and specific surface areas are within the same magnitude. Detailed electrochemical studies under strongly alkaline conditions revealed that the HER catalytic performance of the three nickel sulfides followed this order: Ni<sub>3</sub>S<sub>2</sub> > NiS<sub>2</sub> > NiS. The highest HER activity of Ni<sub>3</sub>S<sub>2</sub> is attributed to the combined effect of large electrochemically active surface area, high conductivity, and unique surface chemistry beneficial for water dissociation, which is a critical step for H<sub>2</sub> evolution under strongly alkaline condition. To the best of our knowledge, this is the first comparative study of the electrocatalytic HER performance of three crystalline nickel sulfides under strongly alkaline conditions.

## Experimental section

### Materials

Nickel acetate tetrahydrate, sulfur, oleylamine, Nafion solution (5wt% in alcohols), and ethanol were all purchased from commercial vendors and used directly without any further purification. Water was deionized (18 MΩ) with a Barnstead E-Pure system.

### Catalyst preparation

All three nickel sulfides were synthesized via a convenient microwave-assisted solvothermal method. In a typical synthesis of NiS, 1 mmol nickel acetate and 10 mL oleylamine were added into a 35 mL microwave reactor tube, followed by sonication for at least 30 min till a clear blue solution was obtained. Subsequently, 1.5 mmol sulfur powder was added to the solution and the resulting mixture was stirred till sulfur was dissolved completely. The mixture was microwave heated at 260 °C for 10 min, followed by cooling down to room temperature gradually. The reaction mixture was centrifuged and the solid product was washed with copious amount of

ethanol to remove residual sulfur and solvents. The final product was dried and stored under vacuum. NiS<sub>2</sub> and Ni<sub>3</sub>S<sub>2</sub> were synthesized in a similar fashion, except the added amounts of sulfur were adjusted to be 10 and 0.7 mmol, respectively.

### Catalyst characterization.

Powder X-ray diffractions were recorded on a Rigaku MiniflexII Desktop X-ray diffractometer. Scanning electron microscopy (SEM) images were collected on a FEI QUANTA FEG 650 (FEI, USA). Elemental analysis of nickel and sulfur was obtained on a Thermo Electron iCAP inductively coupled plasma spectrophotometer. Surface area results were measured by nitrogen sorption isotherms on an Autosorb iQ automated gas sorption analyzer (Quantachrome Instruments, USA). Before measurements, the samples were degassed under vacuum at 200 °C for 6 h. The Brunauer-Emmett-Teller (BET) method was utilized to calculate the specific surface area. X-ray photoelectron spectroscopy analyses were conducted on a Kratos Axis Ultra instrument (Chestnut Ridge, NY). The samples were affixed on a stainless steel Kratos sample bar, loaded into the instrument's load lock chamber, and evacuated to  $5 \times 10^{-8}$  torr before it was transferred into the sample analysis chamber under ultrahigh vacuum conditions ( $\sim 10^{-10}$  torr). X-ray photoelectron spectra were taken using the monochromatic Al K $\alpha$  source (1486.7 eV) at a  $300 \times 700$  μm spot size. Low resolution survey and high resolution region scans at the binding energies of interest were taken for each sample. To minimize charging, samples were flooded with low-energy electrons and ions from the instrument's built-in charge neutralizer. The samples were first sputter cleaned inside the analysis chamber with 1 keV Ar<sup>+</sup> ions for 30 seconds to remove adventitious contaminants and surface oxides. Data were analyzed using CasaXPS software, and energy corrections on high resolution scans were calibrated by referencing the C 1s peak of adventitious carbon to 284.5 eV.

### Electrochemical measurements.

For electrochemical measurements of each catalyst, 4 mg catalyst was mixed with 1.16 mL ethanol, 0.8 mL water, and 0.04 mL 5% Nafion solution. The mixture was sonicated for at least 30 min till a black homogeneous catalyst ink was obtained. 2.5 μL catalyst ink was deposited on the surface of a rotating disk glassy carbon electrode or a carbon paste electrode for 4 times in order to obtain an electrode surface with evenly distributed catalyst. The catalyst-loaded electrode was dried and stored under vacuum at room temperature. Electrochemical experiments were performed on a Gamry Interface 1000 potentiostat workstation with a three-electrode cell system. A rotating disk glassy carbon electrode ( $d = 3$  mm,  $S = 0.07065$  cm<sup>2</sup>) coated with the nickel sulfide catalyst ink was used as the working electrode, a Ag/AgCl (sat. KCl) electrode (CH Instruments) as the reference electrode, and a Pt wire as the counter electrode. The reference electrode in aqueous media was calibrated with ferrocenecarboxylic acid whose Fe<sup>3+/2+</sup> couple is +0.284 V vs SCE. All potentials reported in the paper were converted to vs RHE (reversible hydrogen electrode). iR (current times internal resistance) correction was applied for linear sweep voltammetry and controlled potential electrolysis

experiments to account for the voltage drop between the reference and working electrodes using Gamry Framework™ Data Acquisition Software 6.11. The linear sweep voltammetry experiments were conducted in N<sub>2</sub> saturated 1.0 M KOH electrolyte at a scan rate of 2 mV/s and a rotating speed of 2000 rpm. Electric impedance spectroscopy measurements in deaerated 1.0 M KOH were carried out in the same configuration at multiple potentials from 10<sup>5</sup> to 0.1 Hz with an AC potential amplitude of 30 mV. The durability of each catalyst for electrocatalytic H<sub>2</sub> evolution in deaerated 1.0 M KOH was assessed via long-term controlled potential electrolysis at -0.377 V vs RHE for 20 h. The working electrode used in long-term electrolysis was a home-made carbon paste electrode. 1 g of graphite powder and 0.25 g of white paraffin wax were loaded into a 25 mL round-bottom flask, followed by the addition of 5 mL hot toluene and sonication for 5 min. The final conductive graphite powder was obtained by solvent removal under vacuum. The carbon paste electrode was made via pressing the carbon paste powder into the void cavity of a home-made electrode linked to a copper wire for alligator connection.

### Theoretical computation methods

The theoretical computations of the three nickel sulfides were performed by using the Vienna ab initio simulation package (VASP) code.<sup>33</sup> The ion-electron interaction is described with the projector augmented wave (PAW) method.<sup>34</sup> Electron exchange correlation is represented by the functional of Perdew-Burke-Ernzerhof (PBE) of generalized gradient approximation (GGA).<sup>35</sup> A cutoff energy of 450 eV was used for the plane-wave basis set. The convergence threshold for structural optimization was set to be 0.02 eV/Å in force. For geometry optimizations, the Brillouin zone was sampled by 7×7×7 Monkhorst-Pack *k*-point mesh, while a larger 19×19×19 *k*-point mesh was used for computing density of states. To take into account the electronic correlation of Ni 3*d* electrons, a simple rotationally invariant DFT+*U* version was used,<sup>36</sup> which has been successfully applied to many strongly correlated systems, including nickel oxides and transition metal sulfides with accurate prediction on structural, magnetic, and surface properties. In this method, parameters *U* and *J* represent on-site Coulomb interaction energy and exchange energy, respectively. For the calculations herein, *U* and *J* were fixed at 4.5 and 0.9 eV, respectively.

### Results and discussion

There are two common forms of NiS: α-NiS and β-NiS. The α-NiS adopts a hexagonal nickel arsenide structure (Figure 1a), wherein each nickel atom is surrounded octahedrally by six sulfur atoms, but also approached fairly closely by two other nickel atoms: the Ni-Ni distance is ~2.68 Å, implying a considerable amount of metal-metal bonding. The second common nickel sulfide is cubic NiS<sub>2</sub> of the pyrite structure (Figure 1b), which contains discrete S<sub>2</sub> units. The S-S distance of those S<sub>2</sub> units is very close to a single S-S bond. This structure can be visualized as a distorted NaCl structure, where

nickel atoms occupy the Na positions while S<sub>2</sub> groups are positioned with their centers at the Cl positions. The heazelwoodite Ni<sub>3</sub>S<sub>2</sub> crystallizes in a rhombohedral structure (Figure 1c), in which each nickel atom sits at a pseudotetrahedral site in an approximately body-centered cubic sulfur lattice. The Ni<sub>3</sub>S<sub>2</sub> units were interconnected by short Ni-S (2.29 Å) and Ni-Ni (2.53 Å) distances, leading to appreciable metal-metal bonding interaction between nickel atoms. The trigonal bipyramidal core of Ni<sub>3</sub>S<sub>2</sub> is also highlighted in Figure 1c. Despite distinctive stoichiometry and structure, all these three nickel sulfides were reported to be active catalysts for electrocatalytic hydrogen production under various conditions.

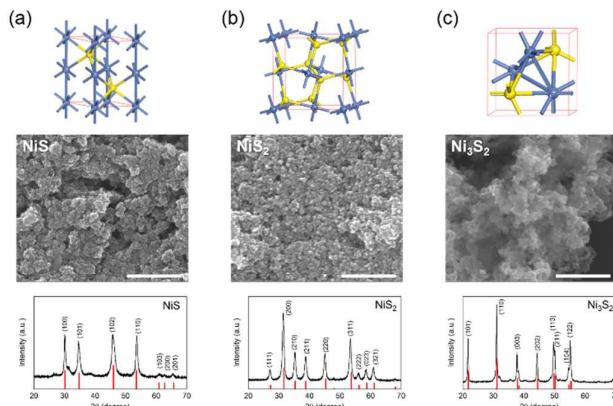


**Figure 1.** Unit cell structure, scanning electron microscopy image, and XRD pattern of (a) NiS, (b) NiS<sub>2</sub>, and (c) Ni<sub>3</sub>S<sub>2</sub>. The red vertical lines in each XRD plot indicate the theoretical pattern. Purple: Ni; yellow: S. Scale bars in those electron microscopy images are 500 nm.

By simply adjusting the molar ratios of starting nickel and sulfur precursors in oleylamine via a microwave-assisted solvothermal method, we were able to obtain well crystalline nickel sulfides of the three crystal structures, hexagonal NiS, cubic NiS<sub>2</sub>, and trigonal Ni<sub>3</sub>S<sub>2</sub>. The purity and crystallinity of these nickel sulfides were first confirmed by X-ray diffraction (XRD) measurements. Figure 1 shows the XRD pattern of each nickel sulfide, NiS (JCPDS No. 02-1280), NiS<sub>2</sub> (JCPDS No. 11-0099), and Ni<sub>3</sub>S<sub>2</sub> (JCPDS No. 44-1418). No impurity peaks were observed in all the three XRD patterns. The sharp and narrow XRD peaks demonstrated the high crystallinity of each nickel sulfide. Based on the Scherrer equation and the most prominent XRD peak of each sample, the calculated crystal sizes of NiS, NiS<sub>2</sub>, and Ni<sub>3</sub>S<sub>2</sub> are 28.6, 25.7, and 55.2 nm, respectively. The morphology of each sample was revealed by scanning electron microscopy (SEM). As included in Figure 1, the SEM images of all the three samples present globular-like nanoparticles with the particle size ranging from 20 to 60 nm, in good agreement with the XRD-derived crystal sizes. The specific surface areas of each sample were measured by nitrogen sorption isotherms (Figure S1). The calculated specific surface areas based on the BET method are 47.6, 21.1, and 37.8 m<sup>2</sup>/g for NiS, NiS<sub>2</sub>, and Ni<sub>3</sub>S<sub>2</sub>, respectively. Elemental analysis was also performed to obtain the molar ratios of Ni : S as 0.51, 1.03, and 1.51 for NiS, NiS<sub>2</sub>, and Ni<sub>3</sub>S<sub>2</sub>, respectively, which are

highly consistent with the corresponding stoichiometric ratios of 0.5, 1.0, and 1.5. Finally, X-ray photoelectron spectroscopy (XPS) was carried out to probe the valence states of nickel and sulfur in each sample (Figure 2). Figure 2a compares the survey spectra of NiS, NiS<sub>2</sub>, and Ni<sub>3</sub>S<sub>2</sub>. All the observed peaks can be assigned to anticipated elements, including Ni, S, and adventitious C. The O signal is likely to be due to the partial oxidation of nickel sulfides during sample preparation for XPS measurements. No other metal impurities were detected. The high-resolution Ni 2p spectra display peaks at 852.9 and 870.1 eV, corresponding to Ni 2p<sub>3/2</sub> and 2p<sub>1/2</sub> features, respectively.<sup>37</sup> The essentially similar binding energies of Ni 2p<sub>3/2</sub> peaks of NiS, NiS<sub>2</sub>, and Ni<sub>3</sub>S<sub>2</sub> were well anticipated, since it is known that the process giving rise to Ni 2p<sub>3/2</sub> peak is mainly of metal character bearing little contribution from the sulfur atoms.<sup>37</sup> Therefore, the nickel 2p<sub>3/2</sub> peaks in nickel sulfides are very close in position to that of metallic nickel (852.5 ± 0.2 eV). The high-resolution S 2p region is included in Figure 2c. The analogous broad feature between 162 to 164 eV for all the three samples is essentially an overlap of S 2p<sub>1/2</sub> and 2p<sub>3/2</sub> peaks, consistent with reported spectra of nickel sulfides.<sup>32</sup> In summary, the aforementioned experimental results, including XRD, SEM, BET, ICP, and XPS unambiguously demonstrate that three crystalline nanoparticles, NiS, NiS<sub>2</sub>, and Ni<sub>3</sub>S<sub>2</sub> have been synthesized successfully. The nanoparticle sizes and specific surface areas are within the same magnitude for all the three nickel sulfides which also bear similar globular morphology.

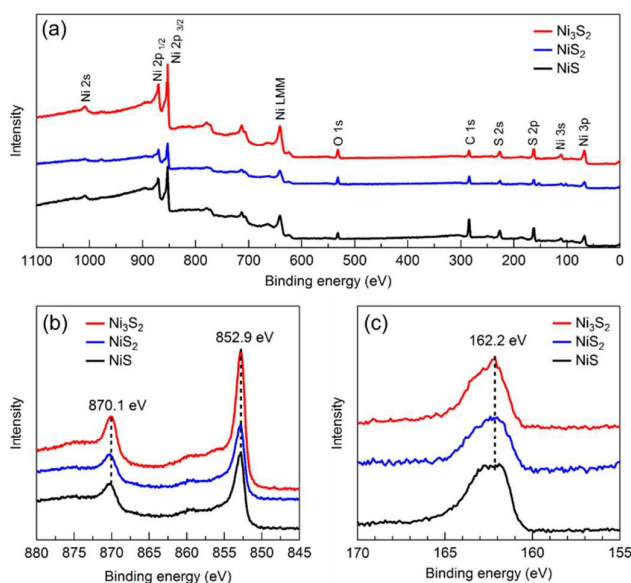


**Figure 2.** XPS spectra of NiS (black), NiS<sub>2</sub> (blue), and Ni<sub>3</sub>S<sub>2</sub> (red): (a) survey, (b) Ni 2p region, and (c) S 2p region.

The electrocatalytic HER performance of the three nickel sulfides was first evaluated via linear sweep voltammetry (LSV) in alkaline electrolyte (1 M KOH). A typical three-electrode configuration was utilized, where the working electrode was prepared by drop casting each catalyst ink onto the surface of a rotating disk glassy carbon electrode with a

loading amount of 0.283 mg/cm<sup>2</sup>. Figure 3 compares the LSV curves of NiS, NiS<sub>2</sub> and Ni<sub>3</sub>S<sub>2</sub> at a scan rate of 2 mV/s and a rotation speed of 2000 rpm. It's worth noting that the rotation rate was varied between 1200 to 2400 rpm for each sample and negligible difference was obtained (Figure S2). As shown in Figure 3a, all three samples enabled electrocatalytic H<sub>2</sub> evolution under negative bias, but there was a marked difference in performance. It is apparent that Ni<sub>3</sub>S<sub>2</sub> exhibited the smallest onset potential and was able to reach a current density of 10 mA/cm<sup>2</sup> at an overpotential ( $\eta$ ) of -335 mV. The activities of NiS<sub>2</sub> and NiS followed that of Ni<sub>3</sub>S<sub>2</sub>, achieving 10 mA/cm<sup>2</sup> at overpotentials of -454 and -474 mV, respectively. The corresponding Tafel plots of these three catalysts are shown in Figure 3b-d. Linear fitting of all the Tafel plots rendered Tafel slopes of 124, 128, and 97 mV/decade for NiS, NiS<sub>2</sub> and Ni<sub>3</sub>S<sub>2</sub>, respectively.

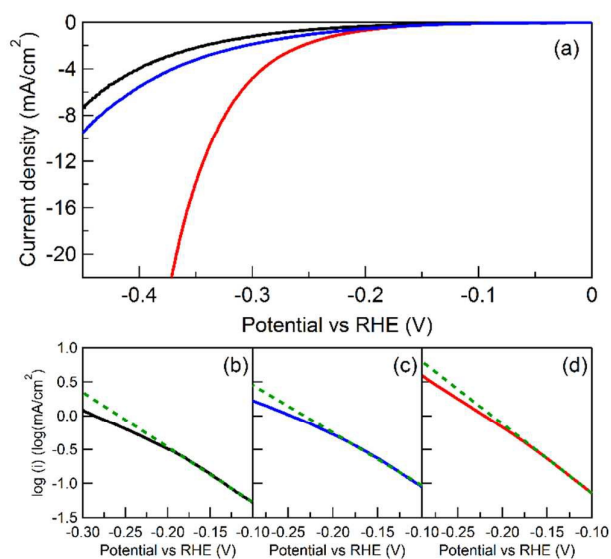


**Figure 3.** (a) Linear sweep voltammograms of NiS (black), NiS<sub>2</sub> (blue), and Ni<sub>3</sub>S<sub>2</sub> (red) collected in 1 M KOH at a scan rate of 2 mV/s and a rotating speed of 2000 rpm and the Tafel plots of NiS (b), NiS<sub>2</sub> (c), and Ni<sub>3</sub>S<sub>2</sub> (d) derived from the corresponding linear sweep voltammograms. Green dashed lines are the linear fittings.

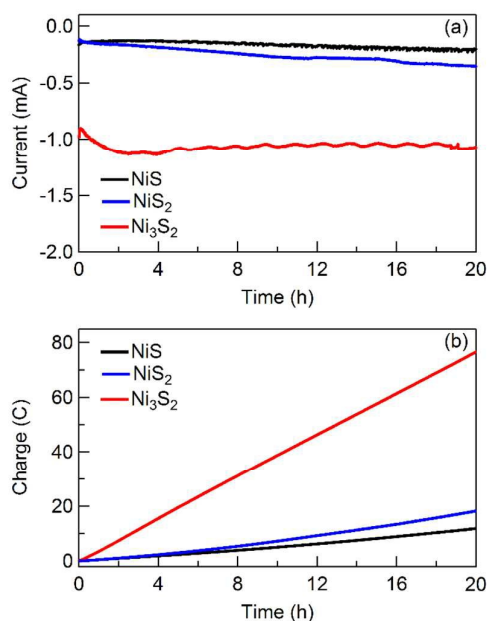


**Figure 4.** Long-term controlled potential electrolysis of the three nickel sulfides in 1.0 M KOH at  $-0.377$  V vs RHE showing the current (a) and accumulated charge (b) over time.

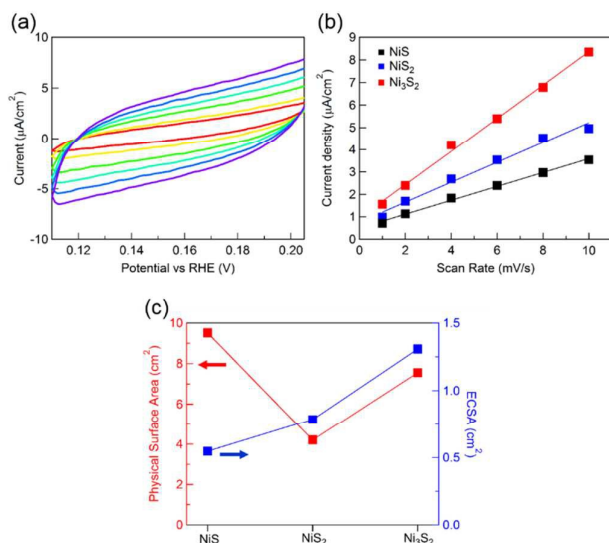


**Figure 5.** (a) Cyclic voltammograms of Ni<sub>3</sub>S<sub>2</sub> in 0.11 – 0.21 V vs RHE at scan rates from 1 to 10 mV/s in 1.0 M KOH. (b) Scan rate dependence of the current densities of NiS, NiS<sub>2</sub> and Ni<sub>3</sub>S<sub>2</sub> (dotted lines) at 0.16 V vs RHE and their corresponding linear fittings (solid lines). (c) Comparison of physical surface area (red) and electrochemically active surface area (ECSA, blue) of NiS, NiS<sub>2</sub>, and Ni<sub>3</sub>S<sub>2</sub>.

Besides catalytic onset and Tafel slope, another crucial factor in the evaluation of an electrocatalyst is its stability under long-term working condition. Thus controlled potential electrolysis was subsequently conducted to assess the robustness of NiS, NiS<sub>2</sub>, and Ni<sub>3</sub>S<sub>2</sub> for HER catalysis in 1 M KOH (Figure 4). At an applied potential of  $-0.377$  V vs RHE,

all the three nickel sulfides exhibited stable cathodic current over 20 h (Figure 4a), resulting in nearly linear charge accumulation versus time (Figure 4b). As expected, Ni<sub>3</sub>S<sub>2</sub> possessed the highest current density and hence produced the largest amount of H<sub>2</sub>, followed by NiS<sub>2</sub> and then NiS. The induction period shown in the chronoamperometric curve of Ni<sub>3</sub>S<sub>2</sub> is likely due to its surface arrangement and the dissolution of nickel oxides on the catalyst surface under cathodic potentials. These results demonstrate that all these nickel sulfides can catalyze H<sub>2</sub> evolution continuously for an extended period of time albeit with different efficiency.

To better understand their HER performance trend and intrinsic activities, we should also consider the electrochemically active surface area (ECSA) of each catalyst, which is well known to significantly impact the electrocatalytic performance of a catalyst. Since it is very challenging to directly measure the absolute ECSA, a widely adopted method is to derive the relative ECSA based on the measurement of double-layer capacitance in the non-Faradaic potential region.<sup>38</sup> It is generally accepted that the double-layer capacitance is linearly proportional to ECSA.<sup>38</sup> The double-layer capacitance of a catalyst can be conveniently deduced from cyclic voltammetry measurements at various scan rates. For instance, the cyclic voltammograms of Ni<sub>3</sub>S<sub>2</sub> in  $-0.11$  to  $-0.23$  V vs RHE at different scan rates are displayed in Figure 5a. Similar cyclic voltammograms could be obtained for NiS and NiS<sub>2</sub> (Figure S3). By plotting the difference in current densities of each anodic and cathodic scans versus the scan rate resulted in a linear relationship for each catalyst (Figure 5b). Linear fitting of these plots produced the capacitance of NiS, NiS<sub>2</sub>, and Ni<sub>3</sub>S<sub>2</sub> as 310, 445, and 741 μF/cm<sup>2</sup>, respectively. Assuming a double-layer capacitance of 40 μF/cm<sup>2</sup> for a smooth working electrode,<sup>39</sup> the roughness factors of these nickel sulfides were calculated to be 7.75 (NiS), 11.13 (NiS<sub>2</sub>), and 18.53 (Ni<sub>3</sub>S<sub>2</sub>). Accordingly, the electrochemically active surface area of NiS, NiS<sub>2</sub>, and Ni<sub>3</sub>S<sub>2</sub> are 0.55, 0.79, and 1.31 cm<sup>2</sup>, respectively. On the other hand, based on the loading amount of each catalyst on the working electrode, their physical surface areas were estimated to be 9.51, 4.21, and 7.56 cm<sup>2</sup> for NiS, NiS<sub>2</sub>, and Ni<sub>3</sub>S<sub>2</sub>, respectively. Figure 5c compares the physical surface areas and ECSA of the three nickel sulfides. Although NiS possessed the largest physical surface area, its ECSA was the smallest. On the other hand, NiS<sub>2</sub> with the smallest physical surface area in fact had a larger ECSA than that of NiS. In agreement with its highest HER activity, Ni<sub>3</sub>S<sub>2</sub> showed the largest ECSA, nearly two times that of NiS<sub>2</sub> and three times that of NiS. It is interesting to note that all the measured ECSAs are smaller than those physical surface areas, which is well anticipated since not all the surface sites are active for HER electrocatalysis. In fact, taking Ni<sub>3</sub>S<sub>2</sub> as an example, only about 17% of its physical surface area is functioning towards H<sub>2</sub> production.

Conductivity of a catalyst is another important factor that affects its overall electrocatalytic performance. Electrochemical impedance spectroscopy (EIS) was conducted to reveal the conductivity of these three nickel sulfides. Figure 6 presents the EIS results of the three samples measured at  $\eta = -257$  mV.

Each Nyquist plot starts at a resistance of 10 – 20  $\Omega$ , which is ascribed to the internal resistance of the strongly alkaline electrolyte. The fitted intrinsic resistance of  $\text{Ni}_3\text{S}_2$  was 118  $\Omega$ , much smaller than those of  $\text{NiS}_2$  (264  $\Omega$ ) and  $\text{NiS}$  (378  $\Omega$ ) and in line with the best HER activity of  $\text{Ni}_3\text{S}_2$ . The Bode plots and corresponding fitting curves are included in Figure S4. As shown in Figure 7, at low frequency region, a diagonal line with a slope of  $\sim 45^\circ$  appears at the end of the EIS spectra of  $\text{NiS}_2$  and  $\text{NiS}$ , implying a substrate-diffusion controlled kinetics, which further suggests that the relatively slow water dissociation plays an important role in the HER mechanism of  $\text{NiS}_2$  and  $\text{NiS}$ .

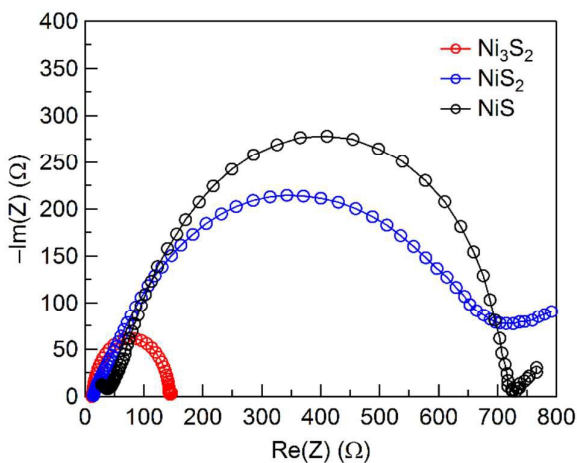


**Figure 6.** Nyquist plots of  $\text{NiS}$  (black),  $\text{NiS}_2$  (blue), and  $\text{Ni}_3\text{S}_2$  (red) at  $-0.257$  V vs RHE.

Finally, we conducted theoretical computation to gain more understanding of the electronic structures of  $\text{NiS}$ ,  $\text{NiS}_2$ , and  $\text{Ni}_3\text{S}_2$ . Owing to their rich electronic properties and diverse applications, nickel sulfides have been a subject of considerable theoretical investigations.<sup>40,41</sup> However, due to the use of differing calculation methods in previous studies, it is difficult to allow a fair comparison on the electronic properties of nickel sulfides of different crystal structures. Herein, density functional theory (DFT) computation of the three nickel sulfides were performed. It should be noted that all the calculations were based on the DFT+U method, in order to obtain more accurate predictions as demonstrated previously.<sup>36</sup> Figure 7 shows the total and site-decomposed density of states for the three nickel sulfides. These plots reveal that the dominant interactions and contributions (in conduction bands and valence bands or at the Fermi level) are Ni 3d – S 3p in character for all the nickel sulfides, whereas S 3s orbitals have little contribution. The most apparent difference in the computed electronic structures among the three nickel sulfides is that  $\text{Ni}_3\text{S}_2$  was found to be metallic with its Fermi level crossing the Ni 3d orbitals, while both  $\text{NiS}$  and  $\text{NiS}_2$  are semiconductors with band gaps of  $\sim 1.1$  and  $\sim 0.4$  eV, respectively. These results are consistent with the EIS measurements. Since a larger band gap leads to higher resistance and hence lower conductivity, the theoretical

computation results further corroborate the HER activities of the three metal sulfides in the order of  $\text{Ni}_3\text{S}_2 > \text{NiS}_2 > \text{NiS}$ .

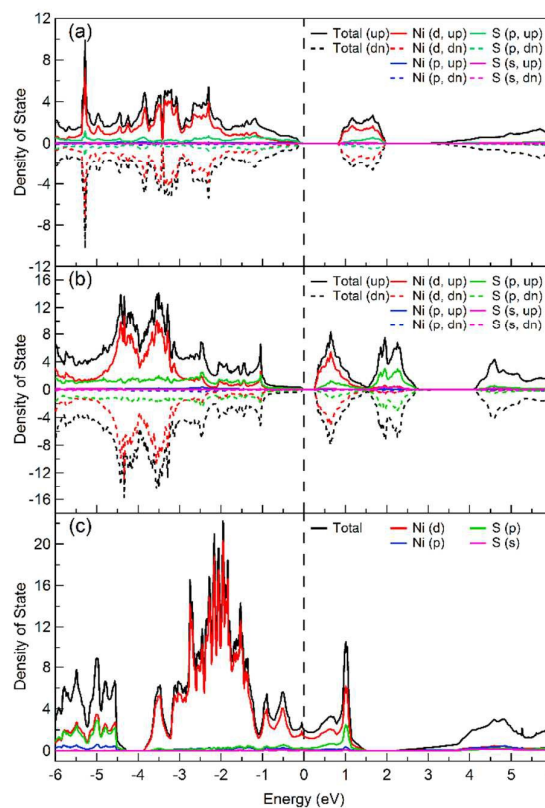


**Figure 7.** The calculated total (per cell) and site-decomposed (per atom) density of states for (a)  $\text{NiS}$ , (b)  $\text{NiS}_2$ , and (c)  $\text{Ni}_3\text{S}_2$ . The Fermi level is denoted by dashed lines at Energy = 0 eV.

## Conclusions

In summary, the crystalline nanoparticles of three nickel sulfides,  $\text{NiS}$ ,  $\text{NiS}_2$ , and  $\text{Ni}_3\text{S}_2$ , were prepared via a facile microwave-assisted solvothermal method. Under the optimized synthetic conditions, the nanoparticle sizes and specific surface areas of these nickel sulfides could be controlled within the same magnitude. A detailed electrochemical study of the  $\text{H}_2$  evolution activities of these nickel sulfides was conducted under strongly alkaline conditions. Theoretical computation was also performed to aid in the understanding of electronic structures of  $\text{NiS}$ ,  $\text{NiS}_2$ , and  $\text{Ni}_3\text{S}_2$ . It was found that  $\text{Ni}_3\text{S}_2$  exhibited the best performance for electrocatalytic HER, which could be rationalized by its large electrochemically active surface area and high intrinsic conductivity.

## Acknowledgements

N.J. acknowledges the Governor's Energy Leadership Scholars Grant of the State of Utah. This work was supported by Utah State University and the Principle Energy Issues Program of the State of Utah. We acknowledge the support from the

Microscopy Core Facility at Utah State University for the SEM work. D. J. acknowledges the support of the University of California, Riverside. The computational work used resources of the National Energy Research Scientific Computing Center, a DOE Office of Science User Facility supported by the Office of Science of the U.S. Department of Energy under Contract DE-AC02-05CH11231.

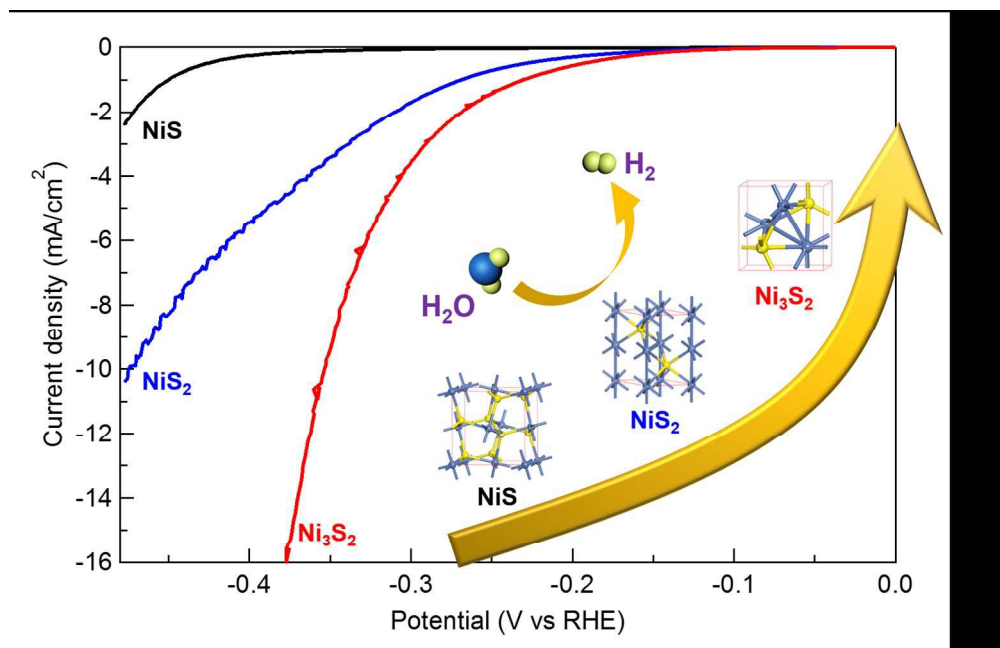
## Notes and references

- N. S. Lewis and D. G. Nocera, *Proc. Natl. Acad. Sci. USA*, 2006, **103**, 15729-15735.
- D. G. Nocera, *Chem. Soc. Rev.*, 2009, **38**, 13-15.
- H. B. Gray, *Nat. Chem.*, 2009, **1**, 7.
- M. G. Walter, E. L. Warren, J. R. McKone, S. W. Boettcher, Q. Mi, E. A. Santori and N. S. Lewis, *Chem. Rev.*, 2010, **110**, 6446-6473.
- (a) T. F. Jaramillo, K. P. Jorgensen, J. Bonde, J. H. Nielsen, S. Horch and I. Chorkendorff, *Science*, 2007, **317**, 100-102; (b) Z. Chen, D. Cummins, B. N. Reinecke, E. Clark, M. K. Sunkara and T. F. Jaramillo, *Nano Letters*, 2011, **11**, 4168-4175; (c) J. D. Benck, Z. Chen, L. Y. Kuritzky, A. J. Forman and T. F. Jaramillo, *ACS Catal.*, 2012, **2**, 1916-1923; (d) J. Kibsgaard, Z. Chen, B. N. Reinecke and T. F. Jaramillo, *Nature Mater.*, 2012, **11**, 963-969; (e) J. D. Benck, T. R. Hellstern, J. Kibsgaard, P. Chakthranont and T. F. Jaramillo, *ACS Catal.*, 2014, 3957-3971.
- (a) D. Merki, S. Fierro, H. Vrubel and X. Hu, *Chem. Sci.*, 2011, **2**, 1262-1267; (b) D. Merki and X. Hu, *Energy Environ. Sci.*, 2011, **4**, 3878-3888; (c) D. Merki, H. Vrubel, L. Rovelli, S. Fierro and X. Hu, *Chem. Sci.*, 2012, **3**, 2515-2525; (d) H. Vrubel, D. Merki and X. Hu, *Energy Environ. Sci.*, 2012, **5**, 6136-6144; (e) H. Vrubel, T. Moehl, M. Gratzel and X. Hu, *Chem. Commun.*, 2013, **49**, 8985-8987; (f) H. Vrubel and X. Hu, *ACS Catal.*, 2013, **3**, 2002-2011; (g) B. Lassalle-Kaiser, D. Merki, H. Vrubel, S. Gul, V. K. Yachandra, X. Hu and J. Yano, *J. Am. Chem. Soc.*, 2015, **137**, 314-321; (h) C. G. Morales-Guio and X. Hu, *Acc. Chem. Res.*, 2014, **47**, 2671-2681.
- M. L. Tang, D. C. Grauer, B. Lassalle-Kaiser, V. K. Yachandra, L. Amirav, J. R. Long, J. Yano and A. P. Alivisatos, *Angew. Chem. Int. Ed.*, 2011, **50**, 10203-10207.
- (a) H. Vrubel and X. Hu, *Angew. Chem. Int. Ed.*, 2012, **51**, 12703-12706; (b) M. D. Scanlon, X. Bian, H. Vrubel, V. Amstutz, K. Schenck, X. Hu, B. Liu and H. H. Girault, *Phys. Chem. Chem. Phys.*, 2013, **15**, 2847-2857.
- W. F. Chen, C. H. Wang, K. Sasaki, N. Marinkovic, W. Xu, J. T. Muckerman, Y. Zhu and R. R. Adzic, *Energy Environ. Sci.*, 2013, **6**, 943-951.
- L. Liao, S. Wang, J. Xiao, X. Bian, Y. Zhang, M. D. Scanlon, X. Hu, Y. Tang, B. Liu and H. H. Girault, *Energy Environ. Sci.*, 2014, **7**, 387-392.
- L. F. Pan, Y. H. Li, S. Yang, P. F. Liu, M. Q. Yu and H. G. Yang, *Chem. Commun.*, 2014, **50**, 13135-13137.
- C. Wan, Y. N. Regmi and B. M. Leonard, *Angew. Chem. Int. Ed.*, 2014, **53**, 6407-6410.
- XH. B. Wu, B. Y. Xia, L. Yu, X.-Y. Yu and X. W. Lou, *Nat. Commun.*, 2015, **6**:6512 doi: 10.1038/ncomms7512.
- J. R. McKone, B. F. Sadtler, C. A. Werlang, N. S. Lewis and H. B. Gray, *ACS Catal.*, 2013, **3**, 166-169.
- Y. Sun, C. Liu, D. C. Grauer, J. Yano, J. R. Long, P. Yang and C. J. Chang, *J. Am. Chem. Soc.*, 2013, **135**, 17699-17702.
- M. S. Faber, M. A. Lukowski, Q. Ding, N. S. Kaiser and S. Jin, *J. Phys. Chem. C*, 2014, **118**, 21347-21356.
- D. Kong, H. Wang, Z. Lu and Y. Cui, *J. Am. Chem. Soc.*, 2014, **136**, 4897-4900.
- H. Zhang, B. Yang, X. Wu, Z. Li, L. Lei and X. Zhang, *ACS Appl. Mater. Interfaces*, 2015, **7**, 1772-1779.
- (a) J. M. McEnaney, J. Chance Crompton, J. F. Callejas, E. J. Popczun, C. G. Read, N. S. Lewis and R. E. Schaak, *Chem. Commun.*, 2014, **50**, 11026-11028; (b) E. J. Popczun, C. G. Read, C. W. Roske, N. S. Lewis and R. E. Schaak, *Angew. Chem. Int. Ed.*, 2014, **53**, 5427-5430; (c) F. H. Saadi, A. I. Carim, E. Verlage, J. C. Hemminger, N. S. Lewis and M. P. Soriaga, *J. Phys. Chem. C*, 2014, **118**, 29294-29300; (d) E. J. Popczun, C. W. Roske, C. G. Read, J. C. Crompton, J. M. McEnaney, J. F. Callejas, N. S. Lewis and R. E. Schaak, *J. Mater. Chem. A*, 2015, **3**, 5420-5425.
- Y. Liang, Q. Liu, A. M. Asiri, X. Sun and Y. Luo, *ACS Catal.*, 2014, **4**, 4065-4069.
- (a) N. Jiang, B. You, M. Sheng and Y. Sun, *Angew. Chem. Int. Ed.*, 2015, **54**, 6251-6254; (b) B. You, N. Jiang, M. Sheng and Y. Sun, *Chem. Commun.*, 2015, **51**, 4252-4255.
- (a) M. Frey, *ChemBioChem*, 2002, **3**, 153-160; (b) F. A. Armstrong, *Curr. Opin. Chem. Biol.*, 2004, **8**, 133-140; (c) J. C. Fontecilla-Camps, A. Volbeda, C. Cavazza and Y. Nicolet, *Chem. Rev.*, 2007, **107**, 4273-4303; (d) S. Canaguier, V. Artero and M. Fontecave, *Dalton Trans.*, 2008, 315-325; (e) A. Le Goff, V. Artero, B. Jousselme, P. D. Tran, N. Guillet, R. Métayé, A. Fihri, S. Palacin and M. Fontecave, *Science*, 2009, **326**, 1384-1387.
- H. Lv, Z. Xi, Z. Chen, S. Guo, Y. Yu, W. Zhu, Q. Li, X. Zhang, M. Pan, G. Lu, S. Mu and S. Sun, *J. Am. Chem. Soc.*, 2015.
- P. D. Tran, S. Y. Chiam, P. P. Boix, Y. Ren, S. S. Pramana, J. Fize, V. Artero and J. Barber, *Energy Environ. Sci.*, 2013, **6**, 2452-2459.
- X.-Y. Yu, L. Yu, H. B. Wu and X. W. Lou, *Angew. Chem. Int. Ed.*, 2015, **54**, 5331-5335.
- L. Yang, X. Wu, X. Zhu, C. He, M. Meng, Z. Gan and P. K. Chu, *App. Surf. Sci.*, 2015, **341**, 149-156.
- H. Zhang, B. Yang, X. Wu, Z. Li, L. Lei and X. Zhang, *ACS Appl. Mater. Interfaces*, 2015, **7**, 1772-1779.
- N. Danilovic, R. Subbaraman, D. Strmcnik, K.-C. Chang, A. P. Paulikas, V. R. Stamenkovic and N. M. Markovic, *Angew. Chem. Int. Ed.*, 2012, **51**, 12495-12498.
- (a) E. J. Popczun, J. R. McKone, C. G. Read, A. J. Biacchi, A. M. Wiltrout, N. S. Lewis and R. E. Schaak, *J. Am. Chem. Soc.*, 2013, **135**, 9267-9270; (b) L. Feng, H. Vrubel, M. Bensimon and X. Hu, *Phys. Chem. Chem. Phys.*, 2014, **16**, 5917-5921; (c) X. Wang, Y. V. Kolen'ko, X.-Q. Bao, K. Kovnir and L. Liu, *Angew. Chem. Int. Ed.*, 2015, DOI: 10.1002/anie.201502577.
- M. S. Faber, R. Dziejczak, M. A. Lukowski, N. S. Kaiser, Q. Ding and S. Jin, *J. Am. Chem. Soc.*, 2014, **136**, 10053-10061.
- C. Tang, Z. Pu, Q. Liu, A. M. Asiri and X. Sun, *Electrochim. Acta*, 2015, **153**, 508-514.
- N. Jiang, L. Bogoev, M. Popova, S. Gul, J. Yano and Y. Sun, *J. Mater. Chem. A*, 2014, **2**, 19407-19414.
- G. Kresse and J. Furthmüller, *Phys. Rev. B*, 1996, **54**, 11169-11186.
- P. E. Blöchl, *Phys. Rev. B*, 1994, **50**, 17953-17979.
- J. P. Perdew, K. Burke and M. Ernzerhof, *Phys. Rev. Lett.*, 1996, **77**, 3865-3868.
- W.-B. Zhang, J. Li and B.-Y. Tang, *J. Chem. Phys.*, 2013, **138**, 244703.
- H. W. Nesbitt, D. Legrand and G. M. Bancroft, *Phys Chem Minerals*, 2000, **27**, 357-366.
- C. C. L. McCrory, S. Jung, I. M. Ferrer, S. M. Chatman, J. C. Peters and T. F. Jaramillo, *J. Am. Chem. Soc.*, 2015, **137**, 4347-4357.
- C. C. L. McCrory, S. Jung, J. C. Peters and T. F. Jaramillo, *J. Am. Chem. Soc.*, 2013, **135**, 16977-16987.

## ARTICLE

Journal Name

- 40 Z. Lu, B. Klein and D. Singh, *Phys. Rev. B*, 1996, **54**, 13542-13545.
- 41 W.-B. Zhang, J. Li, X.-H. Liu and B.-Y. Tang, *Comput. Mater. Sci.*, 2014, **83**, 412-417.



290x185mm (150 x 150 DPI)